# Cooperative Passive Pedestrian Detection and Localization Using a Visible Light Communication Access Network

**HAMID HOSSEINIANFAR (Student Member, IEEE),**
**AND MAITE BRANDT-PEARCE (Senior Member, IEEE)**

Charles L. Brown Department of Electrical and Computer Engineering, University of Virginia, Charlottesville, VA 22904, USA

CORRESPONDING AUTHOR: M. BRANDT-PEARCE (e-mail: mb-p@virginia.edu)

Parts of this work have been presented at IEEE CCNC 2020 [1].

**ABSTRACT** Visible light communication (VLC) systems are promising candidates for future indoor access and peer-to-peer networks. The performance of these systems, however, is vulnerable to line of sight (LOS) link blockage due to objects inside the room. Considering pedestrians as the most common VLC links blocking obstacles, we develop a probabilistic passive pedestrian detection and localization method. Our method takes advantage of the blockage status of VLC LOS links between the user equipment (UE) and transceivers on the ceiling to passively detect a single pedestrian, modeled as a cylinder with a random radius. The VLC network gathers the blockage status and computes the geometry of the LOS link graph through a cooperative scheme between VLC device-equipped users inside the room. We also develop a mathematical framework to obtain an optimum solution for estimating the location and size of the object and conclude with a sub-optimum estimation by simplifying the problem to a quadratic programming approach. Simulation results show that using a $5 \times 5$ grid of transceivers on the ceiling and as few as eight UEs, the root-mean-squared error in estimating the center and radius of the object can be less than 5 cm and 3 cm, respectively.

**INDEX TERMS** Scene-awareness, obstacle detection, visible light communications, shadowing, device free localization (DFL), passive visible light positioning (VLP), crowdsourcing.

## I. INTRODUCTION

THE UBIQUITOUS use of light-emitting diodes (LED) for lighting purposes has motivated researchers to consider visible light communications (VLC) technology in future developments of indoor wireless access networks because of its potential to establish high throughput, secure, and low latency data transmission [2]–[4]. Due to the micron-scale wavelength of light signals, VLC systems facilitate the emergence of other promising technologies, such as indoor localization [5]–[7] and occupancy detection [8]. However, VLC systems are mostly dependent on the line-of-sight (LOS) between transceivers because their signals cannot penetrate through or diffract around ordinary objects such as furniture and humans. This feature makes these systems susceptible to shadowing and blockage of opaque objects in the room, where this effect can lead to nearly 70 dB of extra signal attenuation [9]. This article turns this severe blockage drawback into an opportunity to detect and locate obstacles in the indoor space by using the VLC signals themselves, so as to improve the VLC system performance.

From a communications perspective, most research studies address the LOS blockage problem by introducing robust multiplexing techniques. For example, Guzman *et al.* [10], [11] introduce modulation techniques to decrease the blockage probability while still guaranteeing a tolerable level of co-channel interference for an optical atto-cell network. Adaptive joint modulation is another multiplexing technique that can be used to maximize the throughput of the network, considering the blockage as well as illumination constraints [12]. In both of these techniques, knowing the location and dimensions of the obstacles inside the room enables the network to run a more robust and efficient resource allocation algorithm. This knowledge also paves the way for the design of more efficient cellular structures and handover algorithms.

Indoor sensing and localization approaches using wireless communication infrastructure have recently become a hot research topic. Sensing techniques based on conventional radio frequency (RF) systems such as WiFi, can achieve an accuracy of 0.38 cm for systems based on the 802.11$a/g/n$ standard. The localization accuracy of these techniques is intrinsically limited by the RF wavelength. This means that even a small improvement in accuracy necessitates an exponential increase in both hardware (number of access-points and multiple input multiple output (MIMO) antennas) and computational complexity.

In contrast, VLC systems use light, which has an extremely small wavelength medium for data transmission, and thus provides a higher spatial resolution. It also experiences a more deterministic and stable behavior of the optical wireless channel, leading to superior accuracy compared with RF-based counterpart techniques. Theoretical studies [13]–[15] and experimental demonstrations [5]–[7] verify that visible light-based localization systems outperform RF-based systems by orders of magnitude.

Similarly, initial studies on VLC-based *passive* localization techniques justify the potential for achieving high accuracy. Majeed and Hranilovic [16] introduce a VLC-based passive indoor localization approach where the location of an object is estimated by considering the impulse response between the photodetectors and LEDs on the ceiling. Other recent reflection-based techniques such as [17]–[19], which deploy different sensor arrangements, report promising accuracy. However, due to the tiny cross-area of small objects, i.e., the low sensitivity of the impulse response between sensors, the performance of these techniques is susceptible to the signal-to-noise ratio (SNR) as well as the number of sensors. Li-Tech [20] is another recent VLC-based sensing approach that mainly focuses on object detection and shape classification. This platform considers a framework of sensors surrounding an object and detects the object presence through the variation in the LOS signal blockage between each sensor pair. The shape of the object is also detected and reconstructed using the variation in reflected signals. This technique, which is optimized for the highest achievable shape reconstruction accuracy, deploys a huge set of fixed sensors surrounding the object.

The performance of VLC systems is very sensitive to LOS link blockage. Therefore, a reliable super-accurate joint detection and passive localization technique is necessary to predict the LOS link blockage and take advantage of this acquired knowledge to enhance VLC communication system performance. Considering this strong sensitivity, we hypothesize that VLC links can provide a high detection and parameter estimation performance with minimum required hardware. In addition, the VLC LOS link blockage status is an apt VLC-embedded candidate for sensing a pedestrian in an indoor environment, which merits further investigation.

In this article, we develop a VLC-based passive pedestrian detection and localization algorithm taking advantage of VLC LOS links blockage information. In developing the algorithms, we consider the presence of a single object inside the room, specifically a pedestrian, as they are challenging obstacles that often cause catastrophic shadowing in indoor VLC networks. We consider the LOS blockage between the user equipment (UE) optical transceivers and a network of optical transceivers on the ceiling as the observation dataset. In a cooperative scheme with the VLC users, the VLC network crowdsources the UEs' locations and the blockage status of the resulting LOS links. The algorithm employs this dataset to detect a pedestrian's presence and estimate its location and radius.

In summary, this research study makes the following contributions: (i) we introduce a problem framework based on VLC link blockage information that can be used to address system shadowing challenges. As part of this framework, we develop a scenario for gathering blockage status and computing the geometry of the LOS link graph. (ii) We derive mathematical expressions to find the optimum object location considering the human body's statistical model [21]. We further simplify these expressions to result in a quadratic programming optimization as a viable sub-optimal approach. (iii) We discuss practical considerations and limits; we focus on a solid mathematical solution for a single pedestrian which can be extended to multiple pedestrian scenarios in future work.

The rest of the paper is organized as follows. The state of the arts is discussed in detail in Section II. In Section III, the system model is presented. The cooperative scheme for pedestrian detection and passive localization is derived in Section IV. Numerical results are presented and discussed in Section V. Finally, the paper is concluded in Section VI.

*Notation:* $\vec{\mathbf{a}} = [a_1, a_2]$ is a horizontal vector. The labels $B$ and $NB$ refer to quantities that apply to blocked-links and nonblocked-links, respectively. $\Pr(\cdot)$ and $p(\cdot)$ denote the probability and the probability density function, respectively.

## II. RELATED WORKS

Indoor localization and sensing has been a topic of intense interest throughout the signal processing community. Image-based techniques are the first approaches to attract attention due to their use of off-the-shelf inexpensive hardware. Despite this hardware simplicity, image-based pedestrian detection performance is challenging due to its sensitivity to complex backgrounds, illumination variations, and shadows of objects that are indistinguishable from the object itself [22], [23]. In addition, using images may raise privacy concerns, specifically for residential areas, significantly restricting their usability. Studies on other techniques, such as ultrasonic-based and LiDAR-based indoor sensing techniques, have mainly focused on specific applications like autonomous vehicles and indoor robot navigation. Developing these techniques for indoor sensing requires the installation of a huge number of sensors. Therefore, these approaches are not desirable, specifically LiDAR systems, which are expensive and high-maintenance due to their mechanical components. We thus restrict our attention to non-imaging approaches.

## A. RF-BASED PASSIVE LOCALIZATION

Conventional methods of RF-based passive localization/ positioning (also known as device-free localization) rely on the received signal strength indicator (RSSI), which is available in mainstream wireless off-the-shelf equipment. A comparison of different RF-based approaches relying on RSSI shows that a median accuracy of approximately 2 m is achievable using at least six access points in a typical cluttered indoor environment [24]. Increasing the number of access point nodes to 20 can enhance the median accuracy to 1 m. This performance limitation is due to the randomness of RSSI caused by rich multipath fading and also temporal dynamics indoors [25]–[28]. In the emerging 802.11$a/g/n$ standard, channel state information (CSI) can be extracted from off-the-shelf orthogonal frequency division multiplexing (OFDM) receivers, which provide the subcarrier amplitudes and phases [26], [29]. Taking advantage of the high time/frequency resolution and stability of the CSI, the most recent research on CSI-based localization shows an achievable accuracy of 0.38 m [30], [31] with only one MIMO transmitter and two MIMO receiver nodes.

## B. VISIBLE LIGHT-BASED PASSIVE LOCALIZATION

Visible light-based passive sensing techniques can be divided into two categories (adapted from [32]): (i) general visible light-based (unmodified lighting), with either a device-free object (full passive) [8], [17]–[19], or a device-equipped object [33]–[36], and (ii) VLC-based techniques with an active transmitter and a device-free object [16], [20], [37]–[42].

Techniques in the first category mainly use the RSSI for localization, which makes these systems the most inexpensive choice, specifically for occupancy detection. CeilingSee [8] is a fully passive occupancy detection system that uses reverse-biased LED luminaires as photodetectors for sensing with a accuracy of higher than 90%. By deploying an array of sensors on the wall, Faulkner *et al.* [17] developed a similar technique that could also localize the target based on the variations in the RSSI of the ambient light. This research was extended in [18], [19] with a more efficient algorithm that lead to decimeter-level localization accuracy. However, like their RF-based counterpart, these techniques cannot achieve the full potential accuracy of light since the RSSI is not a feature-rich measurement, i.e., it not unique for each place in the room.

On the other hands, the second category's techniques, which use the VLC infrastructure, provide more distinguishable features for localization. LiSense [37] is the first visible light-based sensing platform that takes advantage of shadowing for sensing, where a set of five LEDs on the ceiling and a grid of 324 photodetectors on the floor are deployed for recognizing human body postures. Starlight [38] is an extention of LiSense where the platform was redesigned to achieve the same accuracy with a much smaller number of photodetectors (e.g., 20) in exchange for more LED panels (e.g., 20).
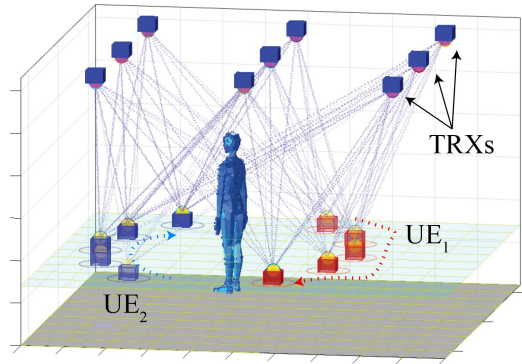


**FIGURE 1.** Illustration of an indoor VLC system where the blockage status of LOS links between nine transceivers on the ceiling and two moving UEs are collected by the network.

In summary, communication infrastructure-based sensing techniques are promising for indoor sensing due to the cutting edge hardware already available in both the user and network equipment. In addition, from a sensing performance perspective, VLC-based techniques show promising results in initial studies. However, VLC specific techniques development is necessary to achieve all the potential sensing capability provided by these systems.

## III. SYSTEM DESCRIPTION

In this work, we consider a typical VLC system with a grid of transceivers (TRX) on the ceiling. The UE can be any device equipped with an optical transceiver, such as a cell phone, a wearable gadget, a laptop dongle, an autonomous agent, or an Internet of things (IoT) device. The algorithm collects blockage information from the signal status at the VLC network central unit, while the UEs may be moving inside the room, as illustrated in Fig. 1. In this study, we neglect shadowing due to UE self-blocking, as most of the devices considered can work remotely, such as autonomous agents and IoT devices. Each UE-ceiling transceiver node pair can mutually sense the signal power from each other and feed this information to the VLC network central unit. The UE-ceiling node links can be numbered arbitrarily, and the measured link status information can be collected as a set of binary indicators as

$$\hat{I}_i = \begin{cases} 0, & \text{link } i \text{ blocked} \\ 1, & \text{link } i \text{ not blocked} \end{cases} \tag{1}$$

for $i = 1, \ldots, L$, where $L$ is the total number of links. $\hat{I}_i$ is an estimate of $I_i$, the geometrically true blockage indicator of the $i$th link status, where the potential measurement error is denoted as $\epsilon$, i.e., $\epsilon = \Pr(I_i \neq \hat{I}_i)$, assumed to be the same for all $i$. This error could happen due to the ambient light, multiuser interference, random receiver orientation, or random reflections in an optical wireless channel. We assume that this error is known in the design of the primary VLC communication system. Given that communications systems are typically designed to meet the hard-decision forward
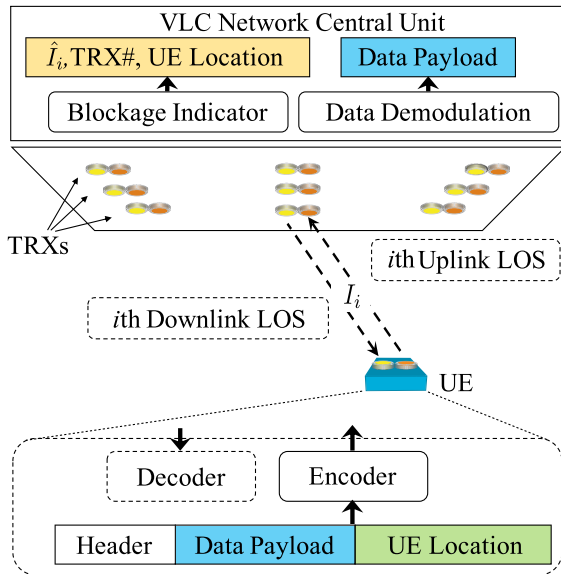
**FIGURE 2.** Schematic view of the *i*th VLC communication link, showing the extraction of the status indicator $I_i$.



**FIGURE 3.** Bird's-eye view illustrating the 2-D LOS blockage information. In this schematic, $I_1 = 0$ and $I_8 = 0$ are the blocked links; therefore, if there are no link status errors, $NB = \{1, 8\}$ and $B = \{2, \ldots, 7\}$.

error correction (HD-FEC) bit-error-rate threshold of $3.8 \times 10^{-3}$, we assume that $\epsilon$ is less than this value.
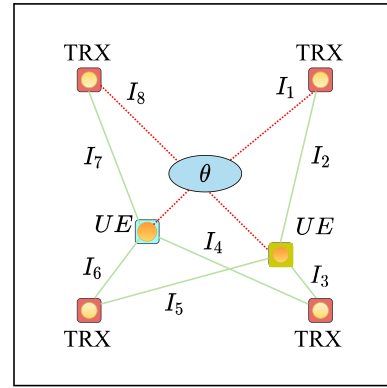
The set of indicators $\hat{\boldsymbol{I}} = \{\hat{I}_i\}_{i=1}^{L}$ can be easily obtained from the RSSI in the preprocessing unit of the communication systems receiver. Fig. 2 illustrates a typical VLC communication system with link blockage status detection. In this system, side information such as the location of the UE can be concatenated to the data packet. The transmitter and receiver nodes can be placed in arbitrary locations on the ceiling. In a typical arrangement considered in this example, the transmitter/receiver pairs are co-located, which leads to the same physical uplink and downlink LOS between each UE and ceiling transceiver node. The link status indicators can be obtained from either the downlinks or uplinks. At the VLC network central unit, in parallel with data packet processing, the information required for object detection is obtained.

Fig. 3 demonstrates a top-view abstraction of a typical VLC scenario, illustrating VLC signal blockage. In the proposed algorithm, the blockage indicators constitute the observed information, which can be partitioned into two subsets $\boldsymbol{B}$ and $\boldsymbol{NB}$ as

$$\boldsymbol{B} = \left\{ i \in 1, \ldots, L | \hat{I}_i = 0 \right\}$$
$$\boldsymbol{NB} = \left\{ i \in 1, \ldots, L | \hat{I}_i = 1 \right\} \qquad (2)$$

To identify all the B-links and NB-links, we assume the VLC system is able to identify the source of the signal at each ceiling node using whatever multiuser access technique employed by the underlying VLC communication system.

By using the link-level information, the proposed algorithm can detect objects that degrade the performance of the communication system for users located near the UEs

themselves, i.e., only objects that interfere in real-time communications are detected. Objects with no VLC users nearby will not block any VLC links and therefore not be detected; however, this is not a problem since these objects cause no impairment to the VLC system.

The fundamental assumptions considered in this article are as follows:

– We assume that the VLC network knows the UEs' locations. This assumption is reasonable considering recent VLC indoor localization techniques that have been shown to provide centimeter-level positioning accuracy [43]. Based on the location of the transceivers on the ceiling and the UEs, the geometric parameters of LOS links can easily be determined.

– The proposed algorithm is piggybacking a typical VLC access network. Therefore, all the parameters corresponding to the PHY and MAC layer, such as ambient light, multiuser interference, and random reflection of the optical wireless channel, are considered in the primary communication system's design and their effects emerge in link status error $\epsilon$.

### A. OBJECT MODEL

Obstacles inside an indoor environment are either background fixed objects such as building pillars, partitioning walls, and decorations, or moving objects, i.e., pedestrians. Although developing a general-purpose sensing algorithm to detect all relevant background and moving objects is necessary for realistic applications, in this article we introduce a sensing technique to sense pedestrians in particular, as this is one of the most challenging obstacles for a VLC network in an indoor environment.

We model the human body as an elliptical cylinder with unknown and random radius and position. In order to guarantee the simplicity and practicality of the proposed algorithm, we assume that the orientation of the ellipse is unknown. Therefore, by considering a uniform distribution for the body's orientation, the resulting object becomes a random circular cylinder; we assume that the distribution of the
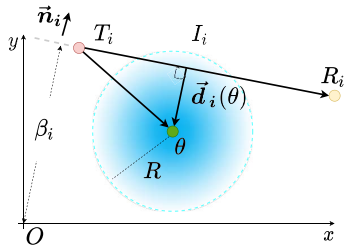
**FIGURE 4.** Distance of an object from a LOS link.



**FIGURE 5.** Realistic measurement scenarios for (a) a poor measurement set, and (b) a richer measurement set, i.e., a larger number of UE connections.

radius of the resulting object in 2 dimensions (2-D) is that of a Gaussian random variable $R \sim \mathcal{N}(\mu_r, \sigma_r)$, where $\mu_r$ and $\sigma_r^2$ are the mean and variance of the object radius, respectively, which are assumed known to the detection algorithm. The statistical model we use is described in detail in [21, Tab. 2]. The other estimation parameter is the horizontal location of the center of object, denoted as $\boldsymbol{\theta} = [\theta_x, \theta_y]^T$.

Fig. 4 illustrates the vector with shortest 2-D Euclidean distance from the $i$th LOS link to an object with radius $R$ located at $\boldsymbol{\theta}$, denoted as $\vec{d}_i(\boldsymbol{\theta})$. Considering the geometrical parameters of the $i$th link, the unit normal vector $\vec{n}_i$, and the distance between the link and the origin of the room's coordinate system, $\beta_i$, we calculate this distance vector as

$$\vec{d}_i(\boldsymbol{\theta}) = (\vec{n}_i \cdot \boldsymbol{\theta} - \beta_i)\vec{n}_i. \qquad (3)$$

The blockage indicator $\hat{I}_i = 0$ used by our algorithm shows that, with high probability, there is an object centered close to the line that defines the LOS of the $i$th link. In contrast, $\hat{I}_i = 1$ indicates that there is no object close to the $i$th link. However, the distances derived using the UE and ceiling transceiver locations are not deterministic due to the random size and location of the object. Considering this fact, the likelihood of the observation $\hat{I}_i = 0$ and $\hat{I}_i = 1$ can be written as

$$\Pr\left(\hat{I}_i = 0 | \boldsymbol{\theta}, \boldsymbol{T}_i, \boldsymbol{R}_i\right) \approx \Pr(I_i = 0 | \boldsymbol{\theta}, \boldsymbol{T}_i, \boldsymbol{R}_i)$$
$$= \Pr\left(R \geq \left|\vec{d}_i(\boldsymbol{\theta})\right|\right) = \delta$$
$$\Pr\left(\hat{I}_i = 1 | \boldsymbol{\theta}, \boldsymbol{T}_i, \boldsymbol{R}_i\right) \approx \Pr(I_i = 1 | \boldsymbol{\theta}, \boldsymbol{T}_i, \boldsymbol{R}_i)$$
$$= \Pr\left(R \leq \left|\vec{d}_i(\boldsymbol{\theta})\right|\right) = 1 - \delta \qquad (4)$$

where

$$\delta \triangleq \int_{\left|\vec{d}_i(\boldsymbol{\theta})\right|}^{+\infty} \frac{e^{-\frac{(r - \mu_r)^2}{2\sigma_r^2}}}{\sqrt{2\pi\sigma_r^2}} dr = Q\left(\frac{\left|\vec{d}_i(\boldsymbol{\theta})\right| - \mu_r}{\sigma_r}\right),$$

$R$ is the random radius of the object and $r$ is a realization of this random variable. $\boldsymbol{T}_i$ and $\boldsymbol{R}_i$ are the locations of the transmitter and the receiver, respectively, corresponding to the $i$th link. The function $Q(\cdot)$ is the Gaussian complementary cumulative distribution function. The approximation above is valid due to the very small value of $\epsilon$ considered in this study, i.e., $\Pr(\hat{I}_i = I_i) = 1 - \epsilon \approx 1$.
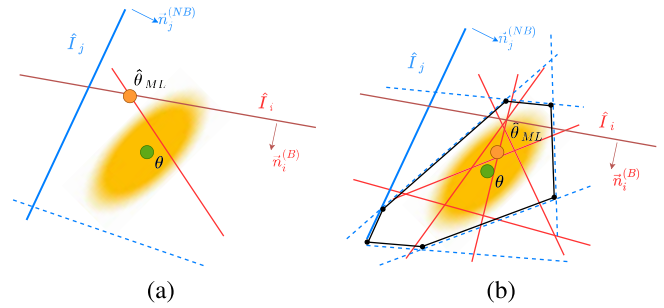
## IV. OBJECT DETECTION AND PARAMETER ESTIMATION ALGORITHM

The proposed algorithm can detect a large object inside the room and estimate its parameters based on the blockage of the LOS signal between each node on the ceiling and the UEs. In developing these solutions, we consider the presence of a single object inside the room. Given this assumption, the detection algorithm simply captures whether there is at least one blocked link in the LOS measurements.

In this section, we discuss the optimum solution for estimating the location and size of the object. We further propose a simple sub-optimal estimation algorithm that has significantly lower complexity. The algorithms estimate the object location in a 2-D plane; they are directly scalable to 3-D object detection and multiple objects scenarios, the details of which are left for future work.

### A. MAXIMUM LIKELIHOOD (ML) PARAMETER ESTIMATION

Given the set of measurements, $\hat{\boldsymbol{I}} = \{\hat{I}_i\}_{i=1}^L$, with elements defined in (1), the optimum estimation for $\boldsymbol{\theta}$, the coordinates of the center of the object on the $xy$-plane, can be obtained based on the ML criterion as

$$\hat{\boldsymbol{\theta}} = \arg\max_{\boldsymbol{\theta}} \left(p\left(\hat{\boldsymbol{I}} | \boldsymbol{\theta}, \boldsymbol{T}_i, \boldsymbol{R}_i, i \in 1, \ldots, L\right)\right) \qquad (5)$$

where $p(\hat{\boldsymbol{I}} | \cdot)$ is the conditional pdf of the observation. Assuming the LOS link geometric parameters $(\vec{n}_i, \beta_i)$ and $\hat{I}_i$ are independent for different $i$'s, the likelihood of all measurements can be written as

$$p\left(\hat{\boldsymbol{I}} | \boldsymbol{\theta}, \boldsymbol{T}_i, \boldsymbol{R}_i\right) = \prod_{i \in \boldsymbol{B}} p\left(\hat{I}_i = 0 | \boldsymbol{\theta}, \boldsymbol{T}_i, \boldsymbol{R}_i\right)$$
$$\times \prod_{j \in \boldsymbol{NB}} p\left(\hat{I}_j = 1 | \boldsymbol{\theta}, \boldsymbol{T}_j, \boldsymbol{R}_j\right) \qquad (6)$$

Obtaining a closed-form solution for this problem is computationally complex. Besides, the ML estimator has drawbacks considering different practical scenarios. For example, there are situations where the number of links near the object is limited, as shown in Fig. 5-(a). This can happen when either the object is located in the corner of the room, or if there are a small number of sensors and measurements. In this situation, the ML estimator can be quite biased

from the true location of the object. Even when there is a larger number of measurements, as shown in Fig. 5-(b), the blocked and non-blocked links do not necessarily preserve symmetry around the center of the object. Therefore, finding a sub-optimal yet more practical and less biased approach to estimating the object's center location is desired.

## B. LEAST SQUARE PARAMETER ESTIMATION

To simplify the ML objective function in (6), we define the log-likelihood function as

$$\ln\left(p\left(\hat{\boldsymbol{I}}|\boldsymbol{\theta}, \boldsymbol{T}_i, \boldsymbol{R}_i\right)\right) = \sum_{i \in \boldsymbol{B}} \ln\left(p\left(\hat{I}_i = 0|\boldsymbol{\theta}, \boldsymbol{T}_i, \boldsymbol{R}_i\right)\right)$$
$$+ \sum_{j \in \boldsymbol{NB}} \ln\left(p\left(\hat{I}_j = 1|\boldsymbol{\theta}, \boldsymbol{T}_i, \boldsymbol{R}_i\right)\right), \quad (7)$$

The expression $\ln(p(\hat{I}_i = 0|\boldsymbol{\theta}, \boldsymbol{T}_i, \boldsymbol{R}_i))$ is strictly decreasing with respect to $|\vec{d}_i(\boldsymbol{\theta})|$ due to the strictly increasing property of $\ln(\cdot)$ and also strictly decreasing property of $Q(\cdot)$ in (4) with respect to their arguments. Contrariwise, $\ln(p(\hat{I}_j = 1|\boldsymbol{\theta}, \boldsymbol{T}_i, \boldsymbol{R}_i))$ is strictly increasing with respect to $|\vec{d}_j(\boldsymbol{\theta})|$. Accordingly, the objective function can be simplified to a constrained least squares problem as

$$\hat{\boldsymbol{\theta}} = \arg\min_{\boldsymbol{\theta}} \sum_{i \in \boldsymbol{B}} \vec{d}_i(\boldsymbol{\theta}) \cdot \vec{d}_i(\boldsymbol{\theta})^T$$
$$s.t.: \left|\vec{d}_j(\boldsymbol{\theta})\right| > D_{min}^{(NB)}, \quad j \in \boldsymbol{NB} \quad (8)$$

where the NB-link measurements can be deployed as constraints. The parameter $D_{min}^{(NB)} = \mu_r + \alpha\sigma_r$ is a guard distance between the predicted object center $\hat{\boldsymbol{\theta}}$ and the NB-links. An initial value of $\alpha = 3$ is used to guarantee that $D_{min}^{(NB)}$ is larger than all possible object's radii. A large value for this parameter helps the algorithm account for close-by NB-links in poor measurement scenarios (shown in Fig. 5-(a)), where the constraint in (8) reduces the parameter estimation error obtained by relying only on B-links. However, in a dense measurements scenario (shown in Fig. 5-(b)), the algorithm might have a null feasible region due to a large given $D_{min}^{(NB)}$. In this case, $\alpha$ can be reduced iteratively until the NB-links' constraints create a non-null feasible region.

The constrained optimization in (8) is a quadratic programming problem that can be solved based on the Karush-Kuhn-Tucker (KKT) criteria [44]. In order to find the global optimum solution to this problem, the optimum point $\boldsymbol{\theta}^*$, we define the Lagrangian function as follows:

$$\mathcal{L}(\boldsymbol{\theta}, \boldsymbol{\lambda}, \boldsymbol{\gamma}) := \sum_{i \in \boldsymbol{B}} (\vec{n}_i \cdot \boldsymbol{\theta} - \beta_i)^2$$
$$+ \sum_{j \in \boldsymbol{NB}} \lambda_j \left[D_{min}^{(NB)} - (\vec{n}_j \cdot \boldsymbol{\theta} - \beta_j)\right]$$
$$+ \sum_{j \in \boldsymbol{NB}} \gamma_j \left[D_{min}^{(NB)} + (\vec{n}_j \cdot \boldsymbol{\theta} - \beta_j)\right] \quad (9)$$

where $\lambda_j$ and $\gamma_j$ are the KKT multipliers. $\boldsymbol{\theta}^*$ is a local minimum of the objective function if there exists a set of

KKT multiplier vectors $\boldsymbol{\lambda}^* = \{\lambda_j^*|j \in \boldsymbol{NB}\}$, and $\boldsymbol{\gamma}^* = \{\gamma_j^*|j \in \boldsymbol{NB}\}$ that satisfy the following conditions, known as KKT conditions:

**Stationarity:**

$$\nabla\mathcal{L}(\boldsymbol{\theta}^*, \boldsymbol{\lambda}^*, \boldsymbol{\gamma}^*) = 0 \quad (10)$$

**Primal and Dual Feasibility:**

$$D_{min}^{(NB)} - (\vec{n}_j \cdot \boldsymbol{\theta}^* - \beta_j) < 0 \quad \lambda_j^* \geq 0$$
$$D_{min}^{(NB)} + (\vec{n}_j \cdot \boldsymbol{\theta}^* - \beta_j) < 0 \quad \gamma_j^* \geq 0$$
$$\text{for} \quad j \in \boldsymbol{NB}. \quad (11)$$

**Complementary Slackness:**

$$\lambda_j^* \left[D_{min}^{(NB)} - (\vec{n}_j \cdot \boldsymbol{\theta}^* - \beta_j)\right] = 0,$$
$$\gamma_j^* \left[D_{min}^{(NB)} + (\vec{n}_j \cdot \boldsymbol{\theta}^* - \beta_j)\right] = 0$$
$$\text{for} \quad j \in \boldsymbol{NB} \quad (12)$$

where $\nabla\mathcal{L}(\boldsymbol{\theta}, \boldsymbol{\lambda}, \boldsymbol{\gamma})$ stands for the gradient of the Lagrangian $\mathcal{L}(\boldsymbol{\theta}, \boldsymbol{\lambda}, \boldsymbol{\gamma})$. The asterisk $*$ identifies the value of the parameter that meets all KKT conditions. The stationary KKT condition in (10) can be written as

$$\frac{\partial\mathcal{L}(\boldsymbol{\theta}, \boldsymbol{\lambda}, \boldsymbol{\gamma})}{\partial\boldsymbol{\theta}} = 2\sum_{i \in \boldsymbol{B}} \vec{n}_i(\vec{n}_i \cdot \boldsymbol{\theta} - \beta_i)$$
$$+ \sum_{j \in \boldsymbol{NB}} (\gamma_j - \lambda_j)\vec{n}_j = 0 \quad (13)$$

To find the local optimum value of $\boldsymbol{\theta}$, we have to solve a linear system of equations with $(2+2[\text{\# of NB-links}])$ unknown parameters that satisfies the feasibility and complementary slackness conditions of (11) and (12), respectively. However, understanding the intuition behind the KKT conditions, and also the geometrical perspective of the optimization problem, helps us reduce unnecessary complexity. Considering the quadratic objective function and linear constraints, we anticipate that $\boldsymbol{\theta}^*$ is either exactly the global optimum of the unconstrained objective function, denoted as $\boldsymbol{\theta}_g$, or on one of the active constraints with closest Euclidean distance from $\boldsymbol{\theta}_g$. With this perspective, we can find a $\boldsymbol{\theta}^*$ that meets the KKT conditions in three steps as follows:

1) **Finding the global minimum $\boldsymbol{\theta}_g$ and corresponding active constraints:** By considering all KKT multipliers to be equal to zero, $\boldsymbol{\theta}_g$ can be obtained from (13) as

$$\boldsymbol{\theta}_g = \mathbf{A}^{-1} \cdot \bar{\boldsymbol{\beta}}$$
$$\text{where} \quad \mathbf{A} = \sum_{i \in \boldsymbol{B}} \vec{n}_i^T \cdot \vec{n}_i, \quad \bar{\boldsymbol{\beta}} = \sum_{i \in \boldsymbol{B}} \beta_i \cdot \vec{n}_i^T \quad (14)$$

The active constraints that must be applied to $\boldsymbol{\theta}_g$ are the constraints that do not satisfy the feasibility condition of (11), which indicate that $\boldsymbol{\theta}_g$ is too close to some NB-link. In this case, the corresponding KKT multipliers are most probably positive values, making the Lagrangian gradient zero on the border of the feasible region, i.e., creating a push vector to keep the object far away from the corresponding NB-link.

2) **Finding the feasible intersection points of active constraints:** In this step, we are looking for active constraints corresponding to $\boldsymbol{\theta_g}$ that are potentially part of the smallest polygon created by NB lines that surround $\boldsymbol{\theta_g}$, as shown in Fig. 5-b. For this purpose, we find the intersection points of the active constraints and check the feasibility condition (11) at these points. The intersection points that meet the feasibility condition and the points satisfying the corresponding active constraints are candidates for local minima. In the case that none of the intersection points meet the condition mentioned above, we are faced with a null feasible region; we then have to decrease $D_{min}^{(NB)}$ and repeat this step.

3) **Solving the simplified KKT conditions linear system of equations:** Considering the quadratic objective function and anticipated linear constraints, all candidates $\boldsymbol{\theta}^*$ are located on either the closest feasible intersection point or the constraints corresponding to $\boldsymbol{\theta}_g$. Therefore, the linear equation (13) can be simplified as

$$\mathbf{A} \cdot \boldsymbol{\theta} + 0.5(\gamma_j - \lambda_j)\vec{\boldsymbol{n}}_j^T = \bar{\boldsymbol{\beta}}, \qquad (15)$$

where $j$ is the index of the closest NB-link to $\boldsymbol{\theta}_g$. The auxiliary equation to solve the optimization problem is the equation of the $j$th line that also satisfies the conditions of (11) and (12).

Considering that the object dimension is small in comparison with the room dimensions, estimating this parameter is difficult because, for a limited number of measurements, the non-blocked links cannot provide enough information on the size of the object; they can only provide an upper bound. However, for the same number of measurements, more blocked links can provide a more accurate estimate of the size of the object. When the center of the object is known, the blocked lines pass through the object from different directions and slice through various parts of the object, as shown in Fig. 5-b. Accordingly, to obtain a general approach for different numbers of measurements, we consider the maximum distance between the estimated center and blocked links as the estimate of the object's radius.

## V. PERFORMANCE ANALYSIS AND NUMERICAL RESULTS

In this section, we analyze the performance of the proposed pedestrian detection and localization algorithm. The performance of this algorithm is affected by several parameters: the number of UE measurements $U$, their geometrical distribution, the size of the network transceiver grid $W \times W$, their exact location on the ceiling, the object's location and dimension, and the link status error $\epsilon$. We consider a typical room without any furnishing to model the LOS signals. Table 1 summarizes the remaining parameters used in our simulations. The UE are assumed to all be at a fixed height from the floor and randomly located in the $(x, y)$ plane inside the room, where the origin of this coordinate system $(0, 0)$ is the center of the room.

We ran a Monte-Carlo simulation to analyze the performance of both detection and localization algorithm.

**TABLE 1.** Simulation parameters.

| Geometric parameters | Value |
|---|---|
| UE height | 0.85 m |
| Ceiling node height | 3 m |
| Room size | $5 \times 5 \times 3$ m |
| **Pillar radius** | 0.4 m |
| **Human body measurement [21]** | |
| Marginal distribution $f_R(r)$ | $\mathcal{N}(\mu_r, \sigma_r)$ |
| Mean object radius $\mu_r$ | 0.13 m |
| Standard deviation of object radius $\sigma_r$ | 0.03 m |

In each trial of this simulation, we generate $U$ number of random positions of UEs. Considering the minimum distance between users in a realistic scenario, i.e., the personal space needed by humans, a Poisson disk sampling method popular in many computer graphics applications is employed for generating the random locations of the UEs [45]. This minimum distance is a function of the number of users and objects inside the room.

For both simulating the link blockage and testing the algorithm, we consider the pedestrian as a cylinder-shaped obstacle with randomly generated parameters $(\boldsymbol{\theta}, R)$, which are unknown to the detection algorithm. In addition, we consider a pillar with a radius that is deterministic but unknown to the algorithm. This simulation runs for $10^4$ trials in a scenario with $\epsilon = 0$ and $10^6$ trials for the $\epsilon \neq 0$ scenarios to ensure a large enough number of random samples are computed for accurate performance evaluation.

To evaluate the performance of our algorithm in detecting a person and the effects of parameter values, we compare the results for a pedestrian to the performance when a large pillar is detected in the room.

### A. DETECTION PERFORMANCE ANALYSIS

The detection algorithm considered in this article recognizes the presence of a single pedestrian if at least one blocked link exists in the LOS link status measurements. To analyze the detection performance, we consider two cases: when the pedestrian is located in the center, $\boldsymbol{\theta} = (0, 0)$ versus on one side of the room, $\boldsymbol{\theta} = (1.5, 0)$ m.

We further consider the error in capturing the LOS link status measurements. Given the hard-decision forward error correction (HD-FEC) minimum threshold of $3.8 \times 10^{-3}$ for communications, we assume the LOS link status measurement error rates range from $10^{-3}$ to $10^{-4}$. To simulate this indicator measurement error, we simply flip the geometrically obtained link status with corresponding error probability to generate the collected link status value expressed in (1).

We evaluate the performance of the detection algorithm based on popular performance measures: the true-positive rate (TPR) and false-positive rate (FPR) [46, Tab. 4.7]. The

TPR and FPR in our study can be calculated as

$$\text{TPR} = \Pr(\boldsymbol{B} \neq \varnothing | \text{Obj. present})$$
$$= 1 - \Pr(\boldsymbol{B} = \varnothing | \text{Obj. present})$$
$$\text{FPR} = \Pr(\boldsymbol{B} \neq \varnothing | \text{Obj. absent})$$
$$= 1 - \Pr(\boldsymbol{B} = \varnothing | \text{Obj. absent}) = 1 - (1 - \epsilon)^{W^2 \times U}$$

$$(16)$$

where $\boldsymbol{B}$ is the set of links measured as blocked, defined in (2), and $\varnothing$ denotes the null set. There is no closed-form expression for TPR as the $\Pr(\boldsymbol{B} = \varnothing | \text{Obj. present})$ is a function of several factors, such as object's size, its location, and the number of UE measurements, i.e., the geometric density of the LOS link graph. However, for a large $U$, the TPR converges to one, as seen below. The FPR is a straightforward function of the link status error $\epsilon$, where at least one of the link status measurements is collected as a blocked link in the absence of the object. For small values of $\epsilon$ considered in this article, the FPR can be simplified as $\text{FPR} \approx W^2 \cdot U \cdot \epsilon$.

Fig. 6-(a) illustrates the relative operating characteristic (ROC) curve for our object detection algorithm. It shows a superb performance for all object types and location scenarios. The detection performance is higher for an object located in the room center, which is expected since a centrally located object is more likely to block LOS links between randomly distributed UEs and uniformly distributed ceiling nodes. The detection performance is more sensitive to the object dimension than the object location; the results for a large pillar outperforms those for a pedestrian object type for both object locations. The link status error $\epsilon$ mainly affects the FPR, where an order of magnitude increase in $\epsilon$ leads to an order of magnitude increase in FPR for similar scenarios; we expect this linear dependency for small $\epsilon$, as discussed above.

Fig. 6-(b) illustrates the overall accuracy of the detection algorithm, i.e., $\text{ACC} = 0.5(\text{TPR} + 1 - \text{FPR})$. For small values of $U$, the accuracy is mainly limited by the TPR, where the more UE measurements, the higher the TPR. However, for a sufficiently large number of UE measurements, the TPR saturates, and the overall accuracy diminishes only slightly due to an increase in $\epsilon$. This behavior is the same for all scenarios, where, for a large number of UE measurements, each plot asymptotically converges to $\text{ACC} \approx 1 - 0.5 W^2 \cdot U \cdot \epsilon$.

## B. PARAMETERS ESTIMATION ERROR
In this section, we evaluate the performance of the passive localization algorithm. We consider the same simulation scenarios as described above. Similar to the detection performance analysis, we conducted parameter estimation simulations for link status error rates of $\epsilon = 10^{-3}$, $\epsilon = 10^{-4}$, and a scenario without error, $\epsilon = 0$. Due to infinitesimal differences between the results, we only show results for the $\epsilon = 0$ case.

Fig. 7 illustrates the root-mean-squared (RMS) error in estimating $\boldsymbol{\theta}$ for two different numbers of transceivers
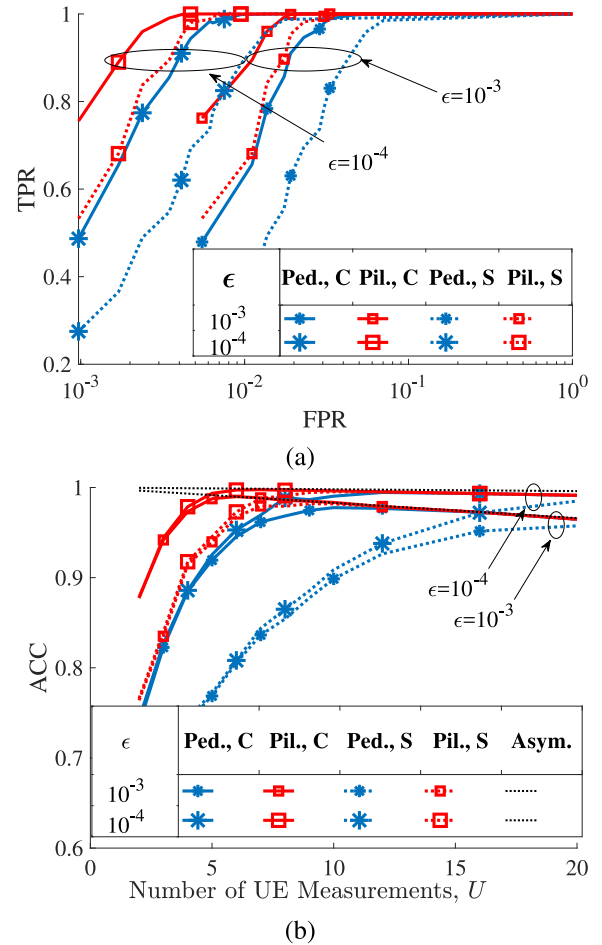


**FIGURE 6.** Simulated detection performance analysis using a 2 × 2 ceiling transceiver grid: a) ROC curve, and b) Accuracy of detection algorithm versus the number of UE measurements. Ped. and Pil. denote whether the object is a pedestrian or pillar, respectively. C stands for the center, $\boldsymbol{\theta} = (0, 0)$, and S for one side of the room, $\boldsymbol{\theta} = (1.5, 0)$, as the object location.

mounted on the ceiling versus the number of UE measurements. Again we tested the algorithm for an object located either in the center or near the edge of the room. For the large pillar, the algorithm can achieve an accuracy of less than 5 cm in estimating the center of the object, $\boldsymbol{\theta}$, using a $5 \times 5$ grid of ceiling transceivers and relying on as few as 8 UE measurements; the estimation error is higher, around 10 cm, for a $2 \times 2$ ceiling transceivers grid, and requires a larger number of observations. Locating a human body is more difficult since the number of blocked links is much smaller compared to larger objects; the algorithm can achieve an accuracy of 10 cm for 14 UE measurements using the denser ceiling transceiver grid.

For large values of $U$ and a $5 \times 5$ transceiver grid, the algorithm collects dense geometric graphs of blocked and non-blocked links. In this case, the smallest polygon created by NB lines tightens around the object, enhancing estimation accuracy of $\boldsymbol{\theta}$, and making the performance insensitive to the object size as long as it is located at the center of the room. However, if the object is located on the side of the
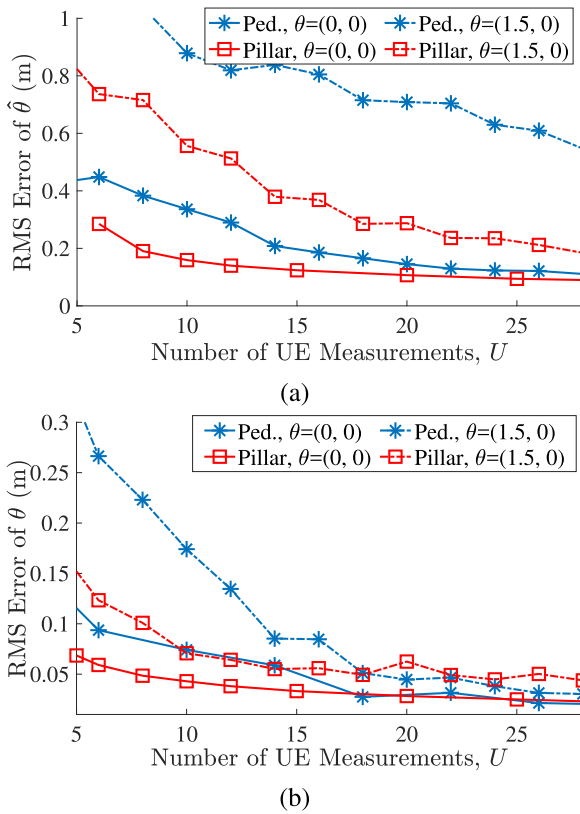
**FIGURE 7.** RMS error in estimating the center of the object $\hat{\theta}$: a) using a 2 × 2 ceiling transceiver grid and b) using a 5 × 5 ceiling transceiver grid.
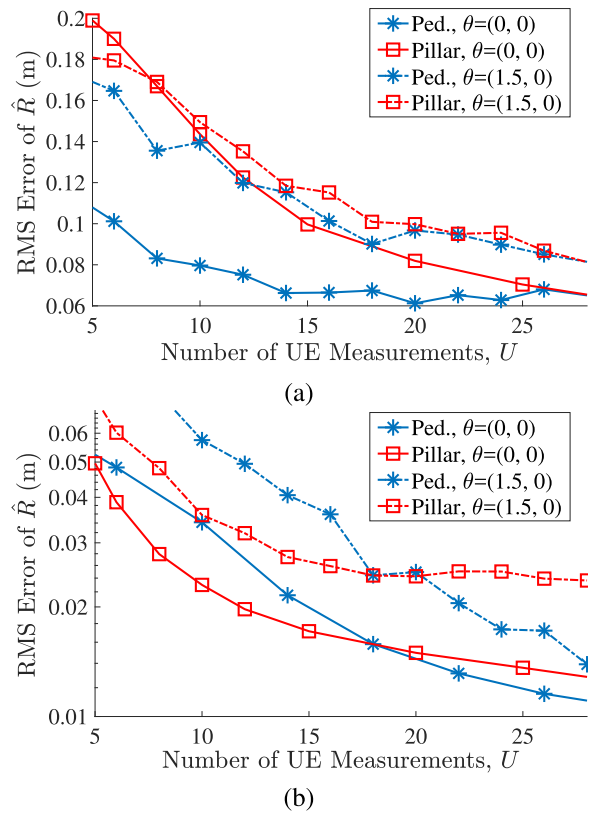


**FIGURE 8.** RMS error in estimating the object radius $\hat{R}$: a) using a 2 × 2 transceiver grid, and b) using a 5 × 5 transceiver grid on the ceiling.

room, both blocked and non-blocked link graphs are subject to an asymmetric displacement as they pass through or surround the object (See Fig. 5-b). Therefore, these asymmetric measurements cause a $\theta$ estimation bias proportional to the object size, leading to a less accurate estimation of the pillar than the pedestrian.

Fig. 8 shows the RMS estimation error of the radius $R$ for a different number of UE measurements, using the same sets of transceivers mounted on the ceiling as for Fig. 7. Similar to the estimation of the $\theta$ parameter, the algorithm can achieve as low as a 1 cm RMS error for estimating $R$ for a 5 × 5 transceiver grid and a RMS error of 6 cm for a 2 × 2 transceiver grid for the large pillar. Depending on the scenario, estimating the radius of the human body may be slightly easier or harder than estimating the radius of a larger object. This is again due to the slight geometric asymmetry in the link graphs; the bias in estimating $\theta$, proportional to object size, propagates as an error in the estimation of the object radius $R$.

By increasing the number of UE measurements, the RMS estimation error for both the center and the radius of the object, $\theta$, and $R$, decrease since the algorithm has more link blockage measurements. For a sufficient number of measurements, the algorithm achieves its lowest RMS estimation error when the object is in the center of the room since the probability of blockage is higher in this region, which leads to more UE measurements for the algorithm to use.

## VI. CONCLUSION AND FUTURE WORK

In this article, cooperative signal processing algorithms are proposed that exploit LOS link blockage information between mobile device optical transceivers and VLC system transceivers on the ceiling to detect and estimate the location and size of a single pedestrian inside the room. Simulation results show that, for a large range of simulation parameters, the detection accuracy remains over 90% and the RMS errors in estimating the center and radius of the object can be as low as a few centimeters.

When the object is a human, how their mobility affects the accuracy of the algorithm is relegated to future studies. Pedestrian mobility affects the performance of both object detection and parameter estimation. From a detection perspective, mobility requires tracking and updating the blockage measurements. The blocked-link status could remain unchanged when the pedestrian moves over a link while it changes when the pedestrian passes through a link. The data-set needs to be updated, and the old measurements need to be validated. From a parameter estimation perspective, the pedestrian mobility could enhance the estimation accuracy if it is combined with a proper tracking algorithm [47]. Developing our signal processing algorithms for a multiple object scenario as well as addressing other realistic constraints such as a limited field of view and self-blockage can also be considered as future work on this research.

## REFERENCES

[1] H. Hosseinianfar and M. Brandt-Pearce, "A cooperative physical layer scene-awareness scheme for visible light communications," in *Proc. IEEE 17th Annu. Consum. Commun. Netw. Conf. (CCNC)*, Las Vegas, NV, USA, 2020, pp. 1–2.

[2] M. Noshad and M. Brandt-Pearce, "Can visible light communications provide Gb/s service?" 2013. [Online]. Available: arXiv:1308.3217.

[3] J. Lian, X. Wang, M. Noshad, and M. Brandt-Pearce, "Optical wireless interception vulnerability analysis of visible light communication system," in *Proc. IEEE Int. Conf. Commun. (ICC)*, Kansas City, MO, USA, 2018, pp. 1–6.

[4] M. Uysal and H. Nouri, "Optical wireless communications—An emerging technology," in *Proc. 16th Int. Conf. Transp. Opt. Netw. (ICTON)*, Graz, Austria, Jul. 2014, pp. 1–7.

[5] T. Tanaka and S. Haruyama, "New position detection method using image sensor and visible light LEDs," in *Proc. 2nd Int. Conf. Mach. Vis. (ICMV)*, Dubai, UAE, Dec. 2009, pp. 150–153.

[6] S.-H. Yang, H.-S. Kim, Y.-H. Son, and S.-K. Han, "Three-dimensional visible light indoor localization using AOA and RSS with multiple optical receivers," *J. Lightw. Technol.*, vol. 32, no. 14, pp. 2480–2485, Jul. 15, 2014.

[7] P. Luo *et al.*, "Experimental demonstration of an indoor visible light communication positioning system using dual-tone multi-frequency technique," in *Proc. 3rd Int. Workshop Opt. Wireless Commun. (IWOW)*, Funchal, Portugal, Sep. 2014, pp. 55–59.

[8] Y. Yang, J. Hao, J. Luo, and S. J. Pan, "Ceilingsee: Device-free occupancy inference through lighting infrastructure based LED sensing," in *Proc. IEEE Int. Conf. Pervasive Comput. Commun. (PerCom)*, Kona, HI, USA, Mar. 2017, pp. 247–256.

[9] Y. Xiang *et al.*, "Human shadowing effect on indoor visible light communications channel characteristics," *Opt. Eng.*, vol. 53, no. 8, 2014, Art. no. 086113.

[10] B. G. Guzman, A. L. Serrano, and V. P. G. Jimenez, "Cooperative optical wireless transmission for improving performance in indoor scenarios for visible light communications," *IEEE Trans. Consum. Electron.*, vol. 61, no. 4, pp. 393–401, Nov. 2015.

[11] B. G. Guzmán, A. A. Dowhuszko, V. P. G. Jiménez, and A. I. Pérez-Neira, "Robust cooperative multicarrier transmission scheme for optical wireless cellular networks," *IEEE Photon. Technol. Lett.*, vol. 30, no. 2, pp. 197–200, Jan. 15, 2018.

[12] J. Lian and M. Brandt-Pearce, "Multiuser MIMO indoor visible light communication system using spatial multiplexing," *J. Lightw. Technol.*, vol. 35, no. 23, pp. 5024–5033, Dec. 1, 2017.

[13] T. Q. Wang, Y. A. Sekercioglu, A. Neild, and J. Armstrong, "Position accuracy of time-of-arrival based ranging using visible light with application in indoor localization systems," *J. Lightw. Technol.*, vol. 31, no. 20, pp. 3302–3308, Oct. 15, 2013.

[14] B. Zhou, A. Liu, and V. Lau, "Performance limits of visible light-based user position and orientation estimation using received signal strength under NLOS propagation," *IEEE Trans. Wireless Commun.*, vol. 18, no. 11, pp. 5227–5241, Nov. 2019.

[15] H. Hosseinianfar and M. Brandt-Pearce, "Performance limits for fingerprinting-based indoor optical communication positioning systems exploiting multipath reflections," *IEEE Photon. J.*, vol. 12, no. 4, pp. 1–16, Aug. 2020.

[16] K. Majeed and S. Hranilovic, "Passive indoor localization for visible light communication systems," in *Proc. IEEE Global Commun. Conf. (GLOBECOM)*, Abu Dhabi, UAE, Dec. 2018, pp. 1–6.

[17] N. Faulkner, F. Alam, M. Legg, and S. Demidenko, "Smart wall: Passive visible light positioning with ambient light only," in *Proc. IEEE Int. Instrum. Meas. Technol. Conf. (I2MTC)*, Auckland, New Zealand, 2019, pp. 1–6.

[18] D. Konings, N. Faulkner, F. Alam, E. M.-K. Lai, and S. Demidenko, "FieldLight: Device-Free indoor human localization using passive visible light positioning and artificial potential fields," *IEEE Sensors J.*, vol. 20, no. 2, pp. 1054–1066, Jan. 2020.

[19] N. Faulkner, F. Alam, M. Legg, and S. Demidenko, "Watchers on the wall: Passive visible light-based positioning and tracking with embedded light-sensors on the wall," *IEEE Trans. Instrum. Meas.*, vol. 69, no. 5, pp. 2522–2532, May 2020.

[20] E. A. Jarchlo *et al.*, "Li-Tect: 3-D monitoring and shape detection using visible light sensors," *IEEE Sensors J.*, vol. 19, no. 3, pp. 940–949, Feb. 2019.

[21] H. Hosseinianfar, J. Lian, and M. Brandt-Pearce, "Probabilistic shadowing model for indoor optical wireless communication systems," in *Proc. IEEE 53rd Asilomar Conf. Signals Syst. Comput.*, Pacific Grove, CA, USA, 2019, pp. 936–941.

[22] A. B. Khalifa, I. Alouani, M. A. Mahjoub, and N. E. B. Amara, "Pedestrian detection using a moving camera: A novel framework for foreground detection," *Cogn. Syst. Res.*, vol. 60, pp. 77–96, May 2020.

[23] J. Z. Liang, N. Corso, E. Turner, and A. Zakhor, "Image based localization in indoor environments," in *Proc. IEEE 4th Int. Conf. Comput. Geospatial Res. Appl.*, San Jose, CA, USA, 2013, pp. 70–75.

[24] D. Konings, F. Alam, F. Noble, and E. M. Lai, "Device-free localization systems utilizing wireless RSSI: A comparative practical investigation," *IEEE Sensors J.*, vol. 19, no. 7, pp. 2747–2757, Apr. 2019.

[25] K. Heurtefeux and F. Valois, "Is RSSI a good choice for localization in wireless sensor network?" in *Proc. IEEE 26th Int. Conf. Adv. Inf. Netw. Appl.*, Fukuoka, Japan, 2012, pp. 732–739.

[26] Z. Yang, Z. Zhou, and Y. Liu, "From RSSI to CSI: Indoor localization via channel response," *ACM Comput. Surveys*, vol. 46, no. 2, pp. 1–32, 2013.

[27] A. Zanella, "Best practice in RSS measurements and ranging," *IEEE Commun. Surveys Tuts.*, vol. 18, no. 4, pp. 2662–2686, 4th Quart., 2016.

[28] D. Konings, N. Faulkner, F. Alam, F. Noble, and E. Lai, "Do RSSI values reliably map to RSS in a localization system?" in *Proc. IEEE 2nd Workshop Recent Trends Telecommun. Res. (RTTR)*, Palmerston North, New Zealand, 2017, pp. 1–5.

[29] D. Halperin, W. Hu, A. Sheth, and D. Wetherall, "Predictable 802.11 packet delivery from wireless channel measurements," *ACM SIGCOMM Comput. Commun. Rev.*, vol. 40, no. 4, pp. 159–170, 2010.

[30] Y. Ma, G. Zhou, and S. Wang, "WiFi sensing with channel state information: A survey," *ACM Comput. Surveys*, vol. 52, no. 3, pp. 1–36, 2019.

[31] K. Qian, C. Wu, Z. Yang, C. Yang, and Y. Liu, "Decimeter level passive tracking with WiFi," in *Proc. 3rd Workshop Hot Topics Wireless*, 2016, pp. 44–48.

[32] Q. Wang and M. Zuniga, "Passive sensing and communication using visible light: Taxonomy, challenges and opportunities," 2017. [Online]. Available: arXiv:1704.01331.

[33] C. Zhang and X. Zhang, "LiTell: Robust indoor localization using unmodified light fixtures," in *Proc. 22nd Annu. Int. Conf. Mobile Comput. Netw.*, 2016, pp. 230–242.

[34] C. Zhang and X. Zhang, "Visible light localization using conventional light fixtures and smartphones," *IEEE Trans. Mobile Comput.*, vol. 18, no. 12, pp. 2968–2983, Dec. 2019.

[35] Y. Hu *et al.*, "Lightitude: Indoor positioning using uneven light intensity distribution," *Proc. ACM Interact. Mobile Wearable Ubiquitous Technol.*, vol. 2, no. 2, pp. 1–25, 2018.

[36] C. Zhang and X. Zhang, "Pulsar: Towards ubiquitous visible light localization," in *Proc. 23rd Annu. Int. Conf. Mobile Comput. Netw.*, 2017, pp. 208–221.

[37] T. Li, C. An, Z. Tian, A. T. Campbell, and X. Zhou, "Human sensing using visible light communication," in *Proc. 21st Annu. Int. Conf. Mobile Comput. Netw.*, 2015, pp. 331–344.

[38] T. Li, Q. Liu, and X. Zhou, "Practical human sensing in the light," in *Proc. 14th Annu. Int. Conf. Mobile Syst. Appl. Serv.*, 2016, pp. 71–84.

[39] E. Lascio, A. Varshney, T. Voigt, and C. Pérez-Penichet, "Poster Abstract: LocaLight—A battery-free passive localization system using visible light," in *Proc. 15th ACM/IEEE Int. Conf. Inf. Process. Sens. Netw. (IPSN)*, Vienna, Austria, 2016, pp. 1–6.

[40] S. Hu, Q. Gao, C. Gong, and Z. Xu, "Efficient visible light sensing in eigenspace," *IEEE Commun. Lett.*, vol. 22, no. 5, pp. 994–997, May 2018.

[41] V. Nguyen, M. Ibrahim, S. Rupavatharam, M. Jawahar, M. Gruteser, and R. Howard, "Eyelight: Light-and-shadow-based occupancy estimation and room activity recognition," in *Proc. IEEE INFOCOM Conf. Comput. Commun.*, Honolulu, HI, USA, 2018, pp. 351–359.

[42] A. A. Al-Hameed, S. H. Younus, A. T. Hussein, M. T. Alresheed, and J. M. Elmirghani, "LiDAL: Light detection and localization," *IEEE Access*, vol. 7, pp. 85645–85687, 2019.

[43] W. Zhang and M. Kavehrad, "Comparison of VLC-based indoor positioning techniques," in *Proc. Broadband Access Commun. Technol. VII*, vol. 8645. San Francisco, CA, USA, 2013, pp. 152–157, doi: 10.1117/12.2001569.

[44] S. Boyd and L. Vandenberghe, *Convex Optimization*. Cambridge, U.K.: Cambridge Univ. Press, 2004.

[45] D. Dunbar and G. Humphreys, "A spatial data structure for fast Poisson-disk sample generation," *ACM Trans. Graph.*, vol. 25, no. 3, pp. 503–508, 2006.

[46] G. James, D. Witten, T. Hastie, and R. Tibshirani, *An Introduction to Statistical Learning*, vol. 112. New York, NY, USA: Springer, 2013. [Online]. Available: https://doi.org/10.1007/978-1-4614-7138-7

[47] G. Bishop and G. Welch, "An introduction to the Kalman filter," *Proc. SIGGRAPH Course*, vol. 8, nos. 27599–23175, p. 41, 2001.

**HAMID HOSSEINIANFAR** (Student Member, IEEE) received the B.Sc. degree in electrical engineering from Shahid Beheshti University, Tehran, Iran, in 2009, and the M.Sc. degree in electrical engineering from the Sharif University of Technology, Tehran, Iran, in 2012. He is currently pursuing the Ph.D. degree in electrical engineering under the supervision of Prof. M. Brandt-Pearce with the University of Virginia, Charlottesville, VA, USA.

**MAITE BRANDT-PEARCE** (Senior Member, IEEE) received the Ph.D. degree in electrical engineering from Rice University in 1993. She is a Professor of electrical engineering and a Vice Provost for faculty affairs with the University of Virginia. She was a Jubilee Professor with Chalmers University, Sweden, in 2014. In addition to co-editing a book entitled *Cross-Layer Design in Optical Networks*, *Springer Optical Networks Series* (2013), and she has over 200 technical publications. Her research interests include free-space optical communications, visible light communications, nonlinear effects in fiber-optics, and cross-layer design of optical networks subject to physical layer degradations. She is the recipient of an NSF CAREER Award and an NSF RIA. She is a co-recipient of Best Paper Awards at ICC 2006 and GLOBECOM 2012. After serving as General Chair of the Asilomar Conference on Signals, Systems and Computers in 2009, she served as a Technical Vice-Chair of GLOBECOM 2016. She had served on the editorial board of the IEEE TRANSACTIONS ON COMMUNICATIONS, IEEE COMMUNICATIONS LETTERS, IEEE/OSA JOURNAL OF OPTICAL COMMUNICATIONS AND NETWORKS, and *Photonic Network Communications* (Springer). She is a member of Tau Beta Pi and Eta Kappa Nu.